Pressure effect on Kohn anomaly and electronic topological transition in single-crystal tantalum

Youjun Zhang, Chao Yang, Ahmet Alatas, Ayman H. Said, Nilesh P. Salke, Jiawang Hong, and Jung-Fu Lin

Phys. Rev. B **100**, 075145 — Published 23 August 2019

DOI: 10.1103/PhysRevB.100.075145

Pressure Effect on Kohn Anomaly and Electronic Topological Transition in Single-Crystal Tantalum

Youjun Zhang[1,4#], Chao Yang[2#], Ahmet Alatas[3], Ayman H. Said[3], Nilesh P. Salke[4], Jiawang Hong[2*], & Jung-Fu Lin[5*]

[1]Institute of Atomic and Molecular Physics, Sichuan University, Chengdu 610065, China.

[2]School of Aerospace Engineering, Beijing Institute of Technology, Beijing 100081, China.

[3]Advanced Photo Source, Argonne National Laboratory, Argonne, Illinois 60439, USA.

[4]Center for High Pressure Science and Technology Advanced Research (HPSTAR), Beijing 100094, China.

[5]Department of Geological Sciences, Jackson School of Geosciences, The University of Texas at Austin, Austin, TX 78712, USA.

[#]Equally contributed to this work.

[*]Correspondence authors. Email: afu@jsg.utexas.edu (J.F.L.) and hongjw@bit.edu.cn (J.H.).

ABSTRACT

The Kohn anomaly and topological change of Fermi surface in *d*-block metals can occur under high pressure with affiliated significant changes in elastic, mechanical, and transport properties. However, our understanding on their origin and associated physical phenomena remains limited both experimentally and theoretically. Here we study the pressure effect on the Kohn anomaly, electronic topological transition (ETT), and the associated anomalies in physical properties of body-centered cubic (*bcc*) single-crystal Tantalum (Ta). The phonon dispersions of Ta crystal were directly measured up to ~47 GPa using high-energy resolution inelastic x-ray scattering in a diamond anvil cell (DAC) with hydrostatic helium medium. A Kohn anomaly in Ta was observed and became significantly stronger at 47.0 GPa at the reduced wave vector of ~0.7 in the longitudinal acoustic mode along the [ξ,0,0] direction. Our theoretical and experimental results indicate that the electron-phonon coupling and Fermi surface nesting mainly contribute to the Kohn anomaly, and the latter plays a dominant role at high pressures of 17–47 GPa. First-principles calculations further reveal an ETT with a topology change of Fermi surface to occur at ~100 GPa in Ta, which causes a softening in the elastic constants (C_{11} and C_{44}) and mechanical properties (shear, Young's, and bulk moduli). Our study shows that the *d*-orbital electrons in Ta play a key role in the stability of its electronic topological structure, where electron doping in Ta could significantly depress its ETT and elastic anomaly at high pressures. It is conceivable that our observed Kohn anomaly and ETT in a representative *bcc* Ta are much more prevalent in *d*-block transition metals under compression than previously thought.

I. INTRODUCTION

The *d*-block transition metals of the periodic table display many interesting yet complex physical properties at high pressure due to their partially-filled *d* outer electronic shells [1-3]. Specifically, compression could significantly affect the *d*-electron interactions and distribution and the atomic vibrations in transition metals [4-6], which may induce some novel phenomena at high pressure, such as Fermi surface nesting [7], strong electron-phonon coupling [8,9], nonadiabatic correction effect [10], and electronic structure transition [11-13], to name a few. The high-pressure properties in *d*-block transition metals have attracted intensive interests as critical benchmarks for first-principles calculations [4,14,15], for importance in syntheses of advanced materials [16-18] as well as for the understanding of the geodynamics [19-22].

The Kohn anomaly is one of the most important anomalies in the phonon dispersions of the transition metals [4,15,23-27], where the lattice vibrations are partly screened by virtual electronic excitations on the Fermi surface. This screening can change rapidly on certain wave vector points of the Brillouin zone so the phonon energy can vary abruptly with the wave vector, determined by the shape of the Fermi surface [27]. Consequently, it usually shows a singularity or sharp dip in the phonon dispersions and a maximum in the phonon linewidth [28,29]. It is believed that the Kohn anomaly can efficiently affect the superconductivity of some conventional superconductors [28], the lattice-dynamical instability [25,30,31], and the formation of spin density waves [32] in elemental metals. Recently, Kohn anomalies were observed in some *d*-block transition metals such as V [31], Nb [28], and Mo [24,33] at various pressure and/or temperature (P-T). However, the mechanism of the Kohn anomaly still lacks of thorough understanding due to the challenge of the direct measurements. In particular, it is necessary to understand the formation and nature of the Kohn anomaly on compression [5], which is expected to hold generally for some *d*-block transition metals.

The Lifshitz type electronic topological transition (ETT) [34] is another interesting issue in high-pressure physics. It was predicted by I. Lifshitz (1960) as the

existence of 2.5 order phase transitions possibly due to a topological change of the Fermi surface in some materials under special conditions. Across the ETT transition, there would be singularities in the third derivatives of the thermodynamic potentials at which the topological transition occurs. Such topology change, ETT, has been observed in many *d* transition metals [11-13,19,35] at variable P-T conditions by theoretical calculations and experiments in the past decades. The electronic band structure, electron-phonon scattering, and/or phonon dispersions could be affected due to ETTs, which can lead to significant changes in their physical properties, such as lattice parameter, elasticity, transport properties, thermodynamic properties, and magnetism [36,37]. For instance, pressure-volume discontinuity [11], elastic constant anomalies [12,38], and lattice constant *c*/*a* ratio anomalies [13] were found at high pressures in *d*-block transition metals across ETTs from first-principles calculations or *in situ* x-ray diffraction in a DAC experiment. It will be important to investigate the Fermi surface behavior, especially its stability, to understand the related physical property anomalies at high pressure.

We chose a typical 5*d* transition metal, tantalum (Ta), to investigate its Kohn anomaly and electronic topological structure because it has a simple and stable *bcc* structure but shows numerous unusual physical properties under high pressure [6,39-46]. Inelastic x-ray scattering (IXS) experiments on polycrystalline Ta in a DAC showed an aggregate shear wave velocity softening at ~100 GPa [41], which was interpreted as a result of the softening in the transverse acoustic phonon mode TA [ξ,0,0] [5]. Meanwhile, a yield strength softening was also observed in powder tantalum at the similar pressure ranges [6]. The phonon dispersion in single-crystal Ta was measured at ambient conditions using inelastic neutron scattering (INS) [47]. The results show that the longitudinal acoustic phonon mode LA[ξ,0,0] at q = ~0.5 to ~0.7 remains flat at ambient pressure. Based on previous density functional theory (DFT) calculations, a phonon dip likely occurs at the wave vector of ~0.6–0.7 in the LA[ξ,0,0] at high pressure [45,48], suggesting a Kohn anomaly in Ta. However, the origin and physical manifestations of the Kohn anomaly remain largely lacking. In addition, first-principles calculations predicted that Ta alloying with neighbors of less

(hafnium) and more (tungsten) *d* electrons could destabilize and stabilize its *bcc* structure at high pressure, respectively [4]. However, the nature of these phenomena in Ta at high pressure still remains unclear. Therefore, it can be an excellent candidate to further understanding the mechanisms of the pressure-induced anomalies in phonon dispersions, electronic band structure, and physical properties from both experimental and theoretical pictures.

Here, we apply high-energy resolution inelastic X-ray scattering (HERIX) in diamond anvil cells to directly investigate the phonon dispersions of single-crystal Ta along high symmetry directions under a hydrostatic compression up to 47 GPa, which is one direct way to extract the information on the lattice dynamics of materials [49,50]. A Kohn anomaly in the longitudinal mode along the [ξ,0,0] direction was clearly observed at 47.0 GPa. Our obtained full elastic moduli by experiments and theoretical calculations show a softening anomaly of C_{11} and C_{44} at high pressure, which is driven by an ETT in compressed Ta. Our density functional theory calculations show that the *d*-orbital electrons in Ta play a key role in the stability of electronic topological structure under high pressure.

II. METHODS OF EXPERIMENT AND COMPUTATION

We carried out HERIX experiments in *bcc*-Ta at pressures of 17.0(5), 42.0(5), and 47.0(5) GPa at room temperature (~300 K) at Sector 30 of the Advanced Photon Source (APS), Argonne National Laboratory. The incident X-ray beam had an energy of 23.724 keV (X-ray wavelength of 0.5224 Å) and overall energy resolution of 1.4 meV of full width at half maximum (FWHM) is achieved using spherically curved analyzer [51,52]. The X-ray beam was focused onto a beam size of 35×15 μm^2 (FWHM) on the sample, which matched our sample size well (a disc with diameter ~45 μm). A high-quality single-crystal Ta with [100] cut (Supplementary Fig. S1 [53]) was used and loaded into a DAC using helium as a pressure medium to ensure hydrostatic conditions (Supplementary Fig. S2 [53]). The single-crystal quality of Ta was checked under high pressure before the HERIX experiments (Supplementary Fig. S3 [53]). The pressures of the sample chamber were determined by the ruby

fluorescence and cross-checked with the sample's equation of state (EOS) from X-ray diffraction of the sample at pressures [54,55]. Technical details are given in Appendix A. The spectra were collected in constant $\boldsymbol{q}$ scans, and the energy values of the phonons $E(\boldsymbol{q})$ were extracted by fitting the measured spectra using the Gaussian function (DAVE2). Representative spectra of the scans in the longitudinal acoustic mode are shown in Supplementary Fig. S4 [53], which were measured in the Brillouin zone around (200) Bragg reflection along the [ξ,0,0] direction at 47.0 GPa.

We performed first-principles calculations based on the DFT for the phonon dispersions and the electronic structure of Ta in the first Brillouin zone at high pressures. The phonon dispersions were calculated using a finite displacement method with the Vienna ab initio simulation package (VASP) code [56,57] and the Phonopy code [58] with the supercell size 8×8×8. To ensure the accuracy of the interatomic forces, we used an energy convergence criterion of 10^{-6} eV and a maximum Hellmann-Feynman force on each atom less than 10^{-3} eVÅ^{-1}. The projector augmented waves approximation and local density approximation were employed to calculate the electronic structure [57,59]. A kinetic energy cutoff of 350 eV and a 40×40×40 Γ-centered k-point (Monkhorst-Pack grid) were used for the primitive cell simulations. As shown in Fig. 1, the calculated phonon dispersions are overall consistent with previous experiments by INS at ambient conditions along the high symmetry directions [47]. The phonons calculated by VASP were cross-checked with Abinit program and the both can reproduce the experiments with minor differences [40,60]. The electron-phonon coupling coefficient and Fermi surface nesting function were calculated using the density functional perturbation theory (DFPT) method implemented in the Abinit code with a norm-conserving Troullier-Martins pseudopotential within LDA for the exchange-correlation function [61,62]. To calculate the electron-phonon coupling properties under high pressure, we used a 40×40×40 Γ–centered *k*-point (Monkhorst-Pack) mesh together with a 10×10×10 *q*-point (Monkhorst-Pack) grid, a Gaussian smearing of 0.001 Ha, and a cut-off energy of 35 Ha. The total energies converged to within 1×10^{-16} Hartree for the ground state and 1×10^{-7} Hartree for a given *q* point.

III. RESULTS AND DISCUSSION

A. Phonon dispersions and pressure effect on the Kohn anomaly.

The measured Ta phonon dispersions for the longitudinal (LA) and transverse acoustic (TA) modes at high pressures and ambient temperature are shown in Fig. 1, along the high symmetry directions [ξ,0,0] (Γ-H) and [ξ,ξ,0] (Γ-N). The phonon energy increases with increasing pressure and our DFT results are generally in good agreement with the HERIX measurements. The LA and TA modes along the Γ-H direction cross each other at a reduced wave vector of $q \approx 0.7$. At 0 and 17 GPa: one can see that the phonon energy from $q = \sim 0.5$ to ~0.7 still remains flat and the phonon dispersions keep the same shape in the [ξ,ξ,0] LA mode. By increasing the pressure up to 47.0 GPa, a Kohn anomaly is clearly observed at $q = \sim 0.7$. These results indicate that compression can enhance the Kohn anomaly in Ta. Our calculated phonon dispersion can reproduce the Kohn anomaly very well up to 47 GPa (Fig. 1). Dispersions along the Γ-N direction at high pressures stiffen but have almost the same shape as the one at ambient conditions. Meanwhile, the phonon linewidth exhibits a sharp peak at the same wave vector as Kohn anomaly occurs, which can be seen in Fig. 2a. At 47.0 GPa, the linewidth becomes broader and more substantial than the one at 17.0 GPa, reaching a maximum of ~5 meV. This broader linewidth at the Kohn anomaly location mainly origins from the electron-phonon coupling, since the phonon-phonon scattering is limited due to the bunching acoustic phonon dispersions [63].

B. Elastic anomaly and mechanical properties.

The elastic constants (C_{11}, C_{12}, and C_{44}) in Ta were obtained from the initial slope of the phonon dispersions of the LA and TA modes along the [ξ,0,0] and [ξ,ξ,0] directions using a linear fitting of the measured inelastic energy shift (E) as a function of the lower momentum transfer (Q) [50] (Supplementary Fig. S5 [53]). Our results are consistent with the previous measurements of powder Ta by IXS at high pressures in Fig. 2b [41]. A likely shear softening C_{44} in Ta was indicated above ~100 GPa by

powder IXS measurements [41]. We calculated the elastic constants of Ta (C_{11}, C_{12}, and C_{44}, respectively) from first-principles at high pressures (solid lines in Fig. 2b). The calculated elastic constants can reproduce our measured results. At pressures of above ~100 GPa (solid-line arrows in Fig. 2b), the calculations show elastic softening for both the C_{11} and C_{44}. The softening of the shear constant C_{44} overall agrees with previous powder-Ta IXS data [41], while the IXS data does not show the C_{11} softening. We also calculated the mechanical properties of Ta at high pressures including shear modulus (G), Young's modulus (E), Bulk modulus (K), and Poisson's ratio (v) in Figs. 3a to 3d. The results show that the shear and Young's modulus have a significantly softening (~20–30%) between 100 GPa and 160 GPa, while the bulk modulus only shows a gentle softening. Correspondingly, the Poisson's ratio shows a pronounced increase of ~17% and reaches a maximum value at ~130 GPa across the ETT.

The calculations of the phonon dispersions to the full high symmetry directions were extended up to 400 GPa, including Γ-H, Γ-N, and Γ-P-H ([ξ,ξ,ξ]) branches, using the same parameters verified by our experiments (Fig. 4a). One can see that the Kohn anomaly at q = ~0.7 in the LA mode along Γ-H becomes stronger with the pressure increase. The Kohn anomaly has the same shape from 100 to 400 GPa without soft phonon mode, indicating no first-order structure phase transition at such high pressures. A phonon anomaly in the longitudinal acoustic phonon along the H-P direction is also observed, which is a common characteristic in most of *bcc* transition metals, such as V [15], Nb [64], Mo [24], Fe [65], Cr [66], and W [67] etc. However, this phonon anomaly along H-P direction still has a stable shape in *bcc*-Ta even up to 400 GPa. Therefore, the full phonon dispersions of high-pressure *bcc* Ta still indicate dynamic stability at ultrahigh pressures of 400 GPa.

C. Electron-phonon coupling and Fermi surface nesting.

To understand the mechanism of the observed Kohn anomaly in compressed Ta, we investigated the electron-phonon interaction and the Fermi surface nesting under high pressure [25,68]. A $\boldsymbol{q}$-dependent electron-phonon coupling (EPC) $\lambda_{\boldsymbol{q}v}$ is given by [69]:

$$\lambda_{\boldsymbol{q}v} = \frac{1}{N_F \omega_{\boldsymbol{q}v}} \sum_{mn,\boldsymbol{K}} w_{\boldsymbol{k}} |g^{v}_{mn}(\boldsymbol{k},\boldsymbol{q})|^2 \delta(\epsilon_{\boldsymbol{k}n}) \delta\left(\epsilon_{\boldsymbol{k}+\boldsymbol{q}m}\right), \quad (1)$$

where δ is the Dirac delta function, $\boldsymbol{k}$ is the wavevector, $\epsilon_{\boldsymbol{k}n}$ is the energy of the electronic state of wave vector $\boldsymbol{k}$ and band index n, and $w_{\boldsymbol{k}}$ is the weights of the $\boldsymbol{k}$-points. $g^{v}_{mn}(\boldsymbol{k},\boldsymbol{q})$ is the electron-phonon matrix element, which represents the changing of the potential felt by the electrons due to the phonon vibration (with crystal momentum $\boldsymbol{q}$, branch v, and frequency ω_{qv}) [70]. We obtained the electron-phonon coupling strength ($\lambda_{\boldsymbol{q}v}$) of the LA mode along the high-symmetry directions, where the Kohn anomaly occurs. We also derived the isotropic electron-phonon coupling parameter (λ_{iso}) in Ta, based on the calculated $\lambda_{\boldsymbol{q}v}$, which is comparable with previous reports (see Supplementary Fig. S6 [53,71-73]). The calculated $\lambda_{\boldsymbol{q}v}$ for the LA mode is shown in Fig. 4b at pressures of 0, 47, and 110 GPa. At ambient pressure, it shows significant electron-phonon coupling with a maximum $\lambda_{\boldsymbol{q}v}$ of 0.41 near q = ~0.7 along the Γ-H direction, which matches well with the wave vector where the phonon energy becomes flat between q = ~0.5 and 0.7, so the coupling may contribute to the occurrence of the Kohn anomaly. By increasing the pressure to 47 GPa and 110 GPa, the coupling peak remains at a fixed wave vector but its strengths show a 10–20% decrease, indicating that pressure depresses the magnitude of the electron-phonon coupling. The decrease of the electron-phonon coupling effect usually lowers down the superconducting critical temperature (T_c) for a conventional superconductor, which is consistent with the recent observation of the T_c reduction in Ta under compression [73]. Therefore, the suppression of the electron-phonon coupling effect at high pressure doesn't contribute to the stronger Kohn anomaly upon compression.

Then, we assessed the Fermi-surface properties in Ta at high pressures. The 3D Fermi surfaces of Ta were mapped at ambient (Fig. 5a) and high pressures (Fig. 5b and Supplementary Fig. S7a [53]) using the WANNIER90 [74]. The nesting of the Fermi surface could be described by a nesting function $\xi(\boldsymbol{q})$, which quantifies the overlap of the Fermi surface with an image of itself shifted by a vector $\boldsymbol{q}$ [25]:

$$\xi(\boldsymbol{q}) = (2/N_k) \sum_{mn,\boldsymbol{K}} \delta(\epsilon_{\boldsymbol{k}n}) \delta\left(\epsilon_{\boldsymbol{k}+\boldsymbol{q}m}\right), \quad (2)$$

where N_k is the number of $\boldsymbol{k}$ points in the summation. Along the Γ-H direction, one can see that a wave vector $\boldsymbol{q}$ connects the parallel Fermi spheres (Fig. 5b), shown as the red arrow in its cross-section of the Fermi surface as well (Supplementary Fig. S8 [53]). Thus, the topology does lend itself to effective nesting. The Fermi surface area for the effective nesting becomes flatter and the density of spanning vectors increases with increasing pressures, which can provide heavier nesting. As a result, the increased nesting effect can greatly enhance the number of possible electronic transitions at the nesting wave vectors compared to other wave vectors, leading to a strong Kohn anomaly in the phonon dispersion. As Fig. 4c shows, the calculated $\xi(\boldsymbol{q})$ has a strong feature along the Γ-H direction, which generally corresponds to the wave vector where the Kohn anomaly occurs. It can be seen that the nesting peak becomes enhanced with pressure increase, contributing to the stronger Kohn anomaly at higher pressure. Furthermore, the wave vector of nesting peak along the Γ-H direction increases from q = ~0.5 to ~0.65 with increasing pressure to 47 GPa, corresponding to the wave vector of the Kohn anomaly gradually changing with pressure increase, as shown in Fig. 1a. This so-called imperfect surface Fermi nesting could cause a Fermi nesting vector ($q = 2k_F + \delta$, δ is the deviation wave vector) slightly deviating from a phonon anomaly wave vector [75,76]. We, therefore, conclude that both the electron-phonon coupling and Fermi surface nesting can contribute to the observed Kohn anomaly at ambient conditions, but the latter can play a much more important role on the enhanced Kohn anomaly at high pressures.

D. Pressure-induced electronic topological transition.

From the 3D Fermi Surfaces of Ta, we observed an ETT of the Fermi surface at 110 GPa (Fig. 5b), where new voids formed near an existing continuous part of the Fermi surface. The voids of the Fermi surfaces grow continuously with increasing pressures, as shown at 125 GPa (Supplementary Fig. S7a [53]). The observed shear velocity (C_{44}) softening in Ta at ~100 GPa [41] occurs very close to the calculated transition pressure of the ETT, indicating that the pressure-induced ETT most likely causes the elastic softening [77] (Appendix B) and the anomalies of mechanical properties as

shown in Fig. 3. The C_{ij} could recover normal behavior upon further pressure increase and after the ETT in Fig. 2b. Besides Ta, ETT-induced elastic anomalies under pressure were also reported on other transition metals, such as Cd [12], Os [38], and Co [78].

The electronic band structure and orbital projected density of state [79] of Ta near the Fermi surface at ambient and high pressures were computed and shown in Figs. 5c and 5d, respectively. It shows that the *d*-electrons play a dominant role near the Fermi surface. Therefore, the observed ETT in Ta at 110 GPa mainly results from the Fermi surface changes of the *d*-electrons. We found that the energy bands around the high symmetry point P shifts upward the Fermi level, but the ETT is not shown clear here. We then particularly investigated the local energy band in Fig. 5e for a better track of the pressure evolution of the ETT, where the new void of Fermi surface is formed (direction along A and B in Fig. 5b). With increasing pressures from 80 to 110 GPa, the result show that the energy band shifts up and crosses the Fermi level at ~100 GPa, which shows the onset of the ETT.

E. The effect of *d*-orbital electrons on the ETT and elastic anomaly.

To further understand the effects of *d*-electrons on the elastic anomaly of Ta under high pressure, we artificially modified the number of the electrons of Ta atom to tune the electronic band structure under pressure [80] and investigated the corresponding change of the elastic constants. An extra 0.15 electrons were doped to the one-unit cell of Ta, and the modified local energy band at 110 GPa is shown in Fig. 5f. Compared with pristine Ta, the electron-doped Ta has a significantly lower energy band, which does not cross the Fermi level. The 3D Fermi surface in electron-doped Ta under pressure was shown in Supplementary Fig. S7b [53]. It indicates no ETT up to 160 GPa and the critical pressure of ETT increases from ~100 GPa to ~180 GPa after doping electrons in Ta. Consequently, the doped electrons could stabilize Ta's electronic topological structure at high pressures, which could depress and postpone the ETT.

The elastic constants were also calculated for the electron-doped Ta (dashed lines in Fig. 2b). It clearly shows that the doped electrons remove the softness of elastic constants at ~100 GPa and postpone to the higher pressure of ~160 GPa (dashed-line arrow), where the ETT occurs in the electron-doped Ta. Our results overall agree with the previous first-principles calculations [4], in which Ta alloying with its nearest neighbor element such as W with a higher *d*-transition metal could remove its elastic softening and stabilize the *bcc* structure under high pressure.

F. Kohn anomaly and ETT in other *d*-block transition metals.

Our studies provide the mechanism and kinetics of the pressure-induced Kohn anomaly and ETT in a representative *d*-block transition metal Ta at high pressures, which may be valid for other *d*-block transition metals. As the structure (*bcc*) and topology of the Fermi surface are very similar to each other in the group-VB elements (V, Nb, and Ta), a common origin for the pressure-induced Kohn anomaly may exist in these metals. A Kohn anomaly at $q \approx 0.7$ in LA mode along the [ξ,0,0] direction in both V [81] and Nb [64] have been observed at ambient conditions, where it becomes much stronger in V under high pressure [31]. Other *bcc* transition metals such as Cr and Mo also show Kohn anomalies [8,24], therefore it is a common phenomenon in *d*-block transition metals, especially at high pressure. The pressure-enhanced Fermi surface nesting plays an important role in the Kohn anomaly of the transition metals.

In addition, the group-VB elements may have a similar ETT at high pressures, which contributes to their elastic anomaly as well. Besides Ta, elastic softening of V was reported by single-crystal IXS experiments [31] and of Nb was predicted by theory[4,77,82], though they occur at different pressure moving down from 5*d* (Ta, ~100 GPa) to 3*d* (V, ~30 GPa) transition metals [4,31]. Therefore, our study here indicates that ETT mainly contributes to the elastic anomaly in the group-VB transition metals under high pressure [5]. On the other hand, V undergoes a structural phase transition from *bcc* to rhombohedral under ~30 GPa (nonhydrostatic compression) to ~62 GPa (hydrostatic compression) at room temperature [83,84], while Nb and Ta have the relatively higher stability of the *bcc* structure than the V

under compression. The earlier shear softening in V likely contributes to the lattice distortion at higher pressures [31]. ETTs have been reported in some other *d*-block transition metals such as 3*d* metals of Fe [19] and Zn [11,85,86], 4*d* metals of Cd [12,35,87], 5*d* metals of Os [13,38]. Therefore, ETT is much more prevalent than our previous thought. Because it can significantly modify the physical and mechanical properties, it is possible to design new materials with improved properties through ETT [88].

IV. CONCLUSION

We have investigated the phonon dispersions of *bcc*-Ta at hydrostatic high pressures using inelastic x-ray scattering measurements and DFT computations. A Kohn anomaly in Ta was observed experimentally in the longitudinal acoustic branch and becomes much more pronounced up to 17–47.0 GPa. The calculated mode-specific electron-phonon coupling strength and Fermi-surface nesting function show peaks at the Kohn anomaly location, where the latter becomes enhanced and the density of spanning vectors increases upon compression. Therefore, our study indicates that the Kohn anomaly in Ta originates from both electron-phonon coupling and Fermi surface nesting, where the Fermi surface nesting plays a more important role on the pressure-enhanced Kohn anomaly. With increasing pressure up to ~100 GPa, we find the occurrence of a topology change of the electronic band structure at Fermi energy (ETT) in Ta, which contributes to the softening of the elastic constants (C_{11} and C_{44}). The shear modulus, Youngs' modulus, and bulk modulus in Ta show the softening with the occurrence of the ETT as well. We also find that the *d*-electron doping in Ta can significantly stabilize the electronic topological structure under compression, which can depress the anomalies in Ta's elasticity and mechanical properties at high pressures. It is believed that the pressure-induced Kohn anomaly and ETT are ubiquitous and important in *d*-block transition metals.

ACKNOWLEDGEMENTS

We acknowledge the support from the National Natural Science Foundation of China (NSFC) (Grant No. 11872077). J.H. acknowledges the support from the NSFC (Grant No. 11572040). Y.Z. acknowledges support from “the Fundamental Research Funds for the central universities” in China. Y.P. Yang and Z.L. Fan completed the FIB cutting at HPSTAR. Thanks to J. Yang, S. Tkachev, M.Q. Hou, S.Y. Fu, H. Yang, and C.W. Zhang for their help with the experiments. Thanks to Freyja O'Toole who read our manuscript and made editorial suggestions. This research used resources of the Advanced Photon Source, a U.S. Department of Energy (DOE) Office of Science User Facility operated for the DOE Office of Science by Argonne National Laboratory under Contract No. DE-AC02-06CH11357. Theoretical calculations were performed using resources of the Texas Advanced Computing Center (TACC) at The University of Texas at Austin and the National Supercomputer Centre in Guangzhou. We acknowledge GeoSoilEnviroCARS (GSECARS) and the High Pressure Collaborative Access Team (HPCAT) at the APS, for the use of their X-ray diffraction and ruby facilities. Use of the gas loading system was supported by GSECARS and COMPRES.

APPENDIX

A: Sample preparation and experimental details.

High-quality *bcc*-Ta single crystal in (100) orientation was purchased from Princeton Scientific Corporation. As shown in Supplementary Fig. S1a [53], the initial size was ~500 μm width and ~150 μm thick. X-ray diffraction (XRD) analysis of the crystal showed the lattice parameter to be 3.3030(10) Å at ambient conditions. Samples were cut to a disc of 45(2) μm diameter and a thickness of 15(1) μm using a focused ion beam (FIB) system [24,89] (FEI VERSA 3D type) at the Center for High Pressure Science and Technology Advanced Research (HPSTAR), Shanghai, as shown in Figs. S1b and S1c. Gallium ions (Ga+) was accelerated through an electrical field of 30 kV to produce a field emission focused ion beam. To protect the crystal quality, we used a small ion beam current of 15 nA to cut the sample. The prepared samples were then retrieved from the initial sample and then cleaned for experiments.

Selected pieces of the FIB-shaped samples were loaded into wide-opening symmetric diamond anvil cells (DACs) with 300 μm or 400 μm culets of diamond, and rhenium gaskets, together with a ruby sphere as the pressure calibrant [90] (Supplementary Fig. S2 [53]). Inert helium gas was used as the pressure medium to ensure hydrostatic compression in the sample chamber and to be more resistant to chemical reactions with the samples at high pressures (Supplementary Fig. S2 [53]).

The quality of each loaded crystal was checked using XRD before HERIX experiments at the 13ID-D station, GeoSoilEnviroConsortium for Advanced Radiation Sources (GSECARS) of the Advanced Photon Source (APS), Argonne National Laboratory (ANL). The incident X-ray beam of 0.3344 Å in wavelength was focused down to ~2 μm in diameter (FWHM). A typical diffraction pattern of a Ta sample at high pressure is recorded using a Pilatus detector as shown in Supplementary Fig. S3 [53]. The image was recorded by rocking the sample from -2° to +2°. The diffraction data in Supplementary Figs. S3a and S3b show that the sample was at 17.0 and 47 GPa [53], respectively, based on the previously determined equation of state of Ta [54]. Our measured lattice parameters in Ta crystal up to 47 GPa are consistent with the previous study in Supplementary Fig. S3d [53,54]. The diffraction spots have a circular shape, and the diffraction spectrum at the [200], [220], and [310] reflections have small FWHM of less than 0.09°, indicating a high quality of the crystal at 17.0 GPa. At higher pressure up to ~47.0 GPa in our experiments, we did not observe evidence of degradation in crystalline quality upon increasing pressure from XRD patterns.

The X-ray beam was focused onto a beam size of 35×15 μm^2 (FWHM) on the sample, which matched our sample size well (a disc with diameter ~45 μm). The pressures of the sample chamber were determined by the ruby fluorescence and cross-checked with the sample's equation of state (EOS) from XRD of the sample at pressures [54]. The pressure uncertainty of the sample was ~0.5 GPa, which was determined by averaging the pressures determined by the lattice parameters and the ruby fluorescence before and after the HERIX experiments, respectively. The incident X-ray beam at Sector 30 of the Advanced Photon Source (APS) had an energy of

23.724 keV (X-ray wavelength of 0.5224 Å) and overall energy resolution of 1.4 meV of full width at half maximum (FWHM) is achieved using spherically curved analyzer [51,52]. The spectra were collected in constant $\boldsymbol{q}$ scans, and the energy values of the phonons $E(\boldsymbol{q})$ were extracted by fitting the measured spectra using the Gaussian function (DAVE2). Supplementary Fig. S4 shows the measured spectra in the longitudinal acoustic mode in the Brillouin zone around (200) Bragg reflection along the [ξ,0,0] direction at 47.0 GPa [53].

B: C_{ij} instability across the ETT

We considered a critical energy E_c, where the Fermi surface undergoes an ETT. The ETT contribution to the elastic constants C_{ij} can be approximately described by an equation [77]:

$$C_{ij} = \frac{1}{V}\frac{\partial^2 E_{band}}{\partial\varepsilon_i \partial\varepsilon_j} \approx \frac{1}{4\pi^2 V|E^*|^{3/2}}\left[-\frac{E_F}{2}\Delta E^{-1/2}\right]\frac{\partial^2 \Delta E}{\partial\varepsilon_i \partial\varepsilon_j}, \quad (3)$$

where E_{band} is the band contribution from the ETT to the total energy, E_F is the energy of Fermi level, ε_i *and* ε_j are the strain components, E^* is a constant parameter, and $\Delta E = E_F - E_c$. When the ETT happens, the difference between E_F and E_c reaches a minimum, so that the C_{ij} can be lowered suddenly. Upon increasing the pressure beyond the ETT, E_F moves away from E_c so that the contribution grows weaker and the C_{ij} recovers to normal behavior.

References

[1] C. Zener, Phys. Rev. **81**, 440 (1951).

[2] V. Iota, J.-H. P. Klepeis, C.-S. Yoo, J. Lang, D. Haskel, and G. Srajer, Appl. Phys. Lett. **90**, 042505 (2007).

[3] R. Slocombe Daniel, L. Kuznetsov Vladimir, W. Grochala, J. P. Williams Robert, and P. Edwards Peter, Philos. Trans. Royal Soc. A **373**, 20140476 (2015).

[4] A. Landa, P. Söderlind, A. V. Ruban, O. E. Peil, and L. Vitos, Phys. Rev. Lett. **103**, 235501 (2009).

[5] A. Landa, P. Söderlind, I. I. Naumov, J. E. Klepeis, and L. Vitos, Computation **6**, 29 (2018).

[6] Q. Jing, Q. Wu, J. Xu, Y. Bi, L. Liu, S. Liu, Y. Zhang, and H. Geng, J. Appl. Phys. **117**, 055903 (2015).

[7] A. Landa, J. Klepeis, P. Söderlind, I. Naumov, O. Velikokhatnyi, L. Vitos, and A. Ruban,

J. Phys.: Condens. Matter **18**, 5079 (2006).
[8] D. Lamago, M. Hoesch, M. Krisch, R. Heid, K. P. Bohnen, P. Böni, and D. Reznik, Phys. Rev. B **82**, 195121 (2010).
[9] D. van der Marel and G. A. Sawatzky, Phys. Rev. B **37**, 10674 (1988).
[10] N. A. Lanzillo, J. B. Thomas, B. Watson, M. Washington, and S. K. Nayak, Proc. Natl. Acad. Sci. USA **111**, 8712 (2014).
[11] Z. Li and J. S. Tse, Phys. Rev. Lett. **85**, 5130 (2000).
[12] V. Srinivasan, B. Godwal, J. C. Grossman, and R. Jeanloz, arXiv preprint arXiv:1511.01989 (2015).
[13]L. Dubrovinsky, N. Dubrovinskaia, E. Bykova, M. Bykov, V. Prakapenka, C. Prescher, K. Glazyrin, H.-P. Liermann, M. Hanfland, and M. Ekholm, Nature **525**, 226 (2015).
[14] O. M. Krasilnikov, M. P. Belov, A. V. Lugovskoy, I. Y. Mosyagin, and Y. K. Vekilov, Comput. Mater. Sci. **81**, 313 (2014).
[15] W. Luo, R. Ahuja, Y. Ding, and H.-k. Mao, Proc. Natl. Acad. Sci. USA, 16428 (2007).
[16] C. Pépin, G. Geneste, A. Dewaele, M. Mezouar, and P. Loubeyre, Science **357**, 382 (2017).
[17] M. Bykov, E. Bykova, G. Aprilis, K. Glazyrin, E. Koemets, I. Chuvashova, I. Kupenko, C. McCammon, M. Mezouar, V. Prakapenka *et al.*, Nat. Commun. **9**, 2756 (2018).
[18] L. Zhang, Y. Wang, J. Lv, and Y. Ma, Nat. Rev. Mater. **2**, 17005 (2017).
[19] K. Glazyrin, L. V. Pourovskii, L. Dubrovinsky, O. Narygina, C. McCammon, B. Hewener, V. Schünemann, J. Wolny, K. Muffler, and A. I. Chumakov, Phys. Rev. Lett. **110**, 117206 (2013).
[20] J.-F. Lin, W. Sturhahn, J. Zhao, G. Shen, H.-k. Mao, and R. J. Hemley, Science **308**, 1892 (2005).
[21]H. K. Mao, J. Xu, V. V. Struzhkin, J. Shu, R. J. Hemley, W. Sturhahn, M. Y. Hu, E. E. Alp, L. Vocadlo, D. Alfè *et al.*, Science **292**, 914 (2001).
[22] B. Martorell, L. Vočadlo, J. Brodholt, and I. G. Wood, Science **342**, 466 (2013).
[23] Y. Xie, J. S. Tse, T. Cui, A. R. Oganov, Z. He, Y. Ma, and G. Zou, Phys. Rev. B **75**, 064102 (2007).
[24] D. L. Farber, M. Krisch, D. Antonangeli, A. Beraud, J. Badro, F. Occelli, and D. Orlikowski, Phys. Rev. Lett. **96**, 115502 (2006).
[25] I. Loa, E. I. Isaev, M. I. McMahon, D. Y. Kim, B. Johansson, A. Bosak, and M. Krisch, Phys. Rev. Lett. **108**, 045502 (2012).
[26] J. Zarestky, C. Stassis, B. N. Harmon, K. M. Ho, and C. L. Fu, Phys. Rev. B **28**, 697 (1983).
[27] W. Kohn, Phys. Rev. Lett. **2**, 393 (1959).
[28] P. Aynajian, T. Keller, L. Boeri, S. Shapiro, K. Habicht, and B. Keimer, Science **319**, 1509 (2008).
[29] X. Zhu, Y. Cao, J. Zhang, E. W. Plummer, and J. Guo, Proc. Natl. Acad. Sci. USA **112**, 2367 (2015).
[30] L. Fast, O. Eriksson, B. Johansson, J. Wills, G. Straub, H. Roeder, and L. Nordström, Phys. Rev. Lett. **81**, 2978 (1998).
[31] D. Antonangeli, D. L. Farber, A. Bosak, C. M. Aracne, D. G. Ruddle, and M. Krisch, Sci. Rep. **6**, 31887 (2016).

[32] S. K. Chan and V. Heine, J. Phys. F.: Metal Physics **3**, 795 (1973).
[33] B. M. Powell, P. Martel, and A. D. B. Woods, Phys. Rev. **171**, 727 (1968).
[34] I. Lifshitz, Sov. Phys. JETP **11**, 1130 (1960).
[35] D. Novikov, M. Katsnelson, A. Trefilov, A. Freeman, N. Christensen, A. Svane, and C. Rodriguez, Phys. Rev. B **59**, 4557 (1999).
[36] Y. M. Blanter, M. Kaganov, A. Pantsulaya, and A. Varlamov, Phys. Rep. **245**, 159 (1994).
[37] A. Varlamov, V. Egorov, and A. Pantsulaya, Adv. Phys. **38**, 469 (1989).
[38] D. Koudela, M. Richter, A. Möbius, K. Koepernik, and H. Eschrig, Phys. Rev. B **74**, 214103 (2006).
[39] A. Dewaele and P. Loubeyre, Phys. Rev. B **72**, 134106 (2005).
[40] Y. Yao and D. D. Klug, Phys. Rev. B **88**, 054102 (2013).
[41] D. Antonangeli, D. L. Farber, A. H. Said, L. R. Benedetti, C. M. Aracne, A. Landa, P. Soderlind, and J. E. Klepeis, Phys. Rev. B **82**, 132101 (2010).
[42] C. J. Wu, P. Söderlind, J. N. Glosli, and J. E. Klepeis, Nat. Mater. **8**, 223 (2009).
[43] B. Albertazzi, N. Ozaki, V. Zhakhovsky, A. Faenov, H. Habara, M. Harmand, N. Hartley, D. Ilnitsky, N. Inogamov, Y. Inubushi *et al.*, Sci. Adv. **3** (2017).
[44] A. Dewaele, M. Mezouar, N. Guignot, and P. Loubeyre, Phys. Rev. Lett. **104**, 255701 (2010).
[45] Z.-L. Liu, L.-C. Cai, X.-R. Chen, Q. Wu, and F.-Q. Jing, J. Phys.: Condens. Matter **21**, 095408 (2009).
[46] J. Hu, C. Dai, Y. Yu, Z. Liu, Y. Tan, X. Zhou, H. Tan, L. Cai, and Q. Wu, J. Appl. Phys. **111**, 033511 (2012).
[47] A. Woods, Phys. Rev. **136**, A781 (1964).
[48] S. Taioli, C. Cazorla, M. J. Gillan, and D. Alfè, Phys. Rev. B **75**, 214103 (2007).
[49] F. Weber, S. Rosenkranz, J.-P. Castellan, R. Osborn, G. Karapetrov, R. Hott, R. Heid, K.-P. Bohnen, and A. Alatas, Phys. Rev. Lett. **107**, 266401 (2011).
[50] J.-F. Lin, J. Wu, J. Zhu, Z. Mao, A. H. Said, B. M. Leu, J. Cheng, Y. Uwatoko, C. Jin, and J. Zhou, Sci. Rep. **4**, 6282 (2014).
[51] A. H. Said, H. Sinn, and R. Divan, J. Synchrotron Radiat. **18**, 492 (2011).
[52] T. Toellner, A. Alatas, and A. Said, J. Synchrotron Radiat. **18**, 605 (2011).
[53]See Supplemental Material at http://link.aps.org/supplemental/ for the sample preparation, representative HERIX results, and calculated electron-phonon coupling parameter and Fermi surfaces in Ta.
[54] A. Dewaele, P. Loubeyre, and M. Mezouar, Phys. Rev. B **69**, 092106 (2004).
[55] H. Cynn and C.-S. Yoo, Phys. Rev. B **59**, 8526 (1999).
[56] G. Kresse and J. Hafner, Phys. Rev. B **47**, 558 (1993).
[57] G. Kresse and J. Furthmüller, Phys. Rev. B **54**, 11169 (1996).
[58] A. Togo, F. Oba, and I. Tanaka, Phys. Rev. B **78**, 134106 (2008).
[59] G. Kresse and J. Furthmüller, Comput. Mater. Sci. **6**, 15 (1996).
[60] M. Černý, P. Řehák, and J. Pokluda, Philos. Mag. **97**, 2971 (2017).
[61] N. Troullier and J. L. Martins, Phys. Rev. B **43**, 1993 (1991).
[62] X. Gonze, J.-M. Beuken, R. Caracas, F. Detraux, M. Fuchs, G.-M. Rignanese, L. Sindic, M. Verstraete, G. Zerah, and F. Jollet, Comput. Mater. Sci. **25**, 478 (2002).
[63] L. Lindsay, D. A. Broido, and T. L. Reinecke, Phys. Rev. Lett. **111**, 025901 (2013).

[64] C. M. Varma and W. Weber, Phys. Rev. B **19**, 6142 (1979).
[65] S. Klotz and M. Braden, Phys. Rev. Lett. **85**, 3209 (2000).
[66] W. Shaw and L. Muhlestein, Phys. Rev. B **4**, 969 (1971).
[67] K. Einarsdotter, B. Sadigh, G. Grimvall, and V. Ozoliņs, Phys. Rev. Lett. **79** (1997).
[68] P. Zhang, S. G. Louie, and M. L. Cohen, Phys. Rev. Lett. **94**, 225502 (2005).
[69] S. Poncé, G. Antonius, P. Boulanger, E. Cannuccia, A. Marini, M. Côté, and X. Gonze, Comput. Mater. Sci. **83**, 341 (2014).
[70] C. Verdi and F. Giustino, Phys. Rev. Lett. **115**, 176401 (2015).
[71] L. Boyer, B. Klein, and D. Papaconstantopoulos, Ferroelectrics **16**, 291 (1977).
[72] A. Al-Lehaibi, J. C. Swihart, W. H. Butler, and F. J. Pinski, Phys. Rev. B **36**, 4103 (1987).
[73] V. V. Struzhkin, Y. A. Timofeev, R. J. Hemley, and H.-k. Mao, Phys. Rev. Lett. **79**, 4262 (1997).
[74] N. Marzari, I. Souza, and D. Vanderbilt, Psi-K newsletter **57**, 129 (2003).
[75] G. H. Gweon, J. D. Denlinger, J. A. Clack, J. W. Allen, C. G. Olson, E. DiMasi, M. C. Aronson, B. Foran, and S. Lee, Phys. Rev. Lett. **81**, 886 (1998).
[76] S. Liu, Phys. Lett. A **27**, 493 (1968).
[77] L. Koči, Y. Ma, A. R. Oganov, P. Souvatzis, and R. Ahuja, Phys. Rev. B **77**, 214101 (2008).
[78] Y. O. Kvashnin, W. Sun, I. Di Marco, and O. Eriksson, Phys. Rev. B **92**, 134422 (2015).
[79] E. Gaidos, C. P. Conrad, M. Manga, and J. Hernlund, Astrophys. J. **718** (2010).
[80] N. Shanthi and D. D. Sarma, Phys. Rev. B **57**, 2153 (1998).
[81]A. Bosak, M. Hoesch, D. Antonangeli, D. L. Farber, I. Fischer, and M. Krisch, Phys. Rev. B **78**, 020301 (2008).
[82] Y. X. Wang, H. Y. Geng, Q. Wu, X. R. Chen, and Y. Sun, J. Appl. Phys. **122**, 235903 (2017).
[83] Z. Jenei, H. Liermann, H. Cynn, J.-H. Klepeis, B. Baer, and W. Evans, Phys. Rev. B **83**, 054101 (2011).
[84] Y. Ding, R. Ahuja, J. Shu, P. Chow, W. Luo, and H.-k. Mao, Phys. Rev. Lett. **98**, 085502 (2007).
[85] S. Klotz, M. Braden, and J. M. Besson, Phys. Rev. Lett. **81**, 1239 (1998).
[86] V. V. Kechin, Phys. Rev. B **63**, 045119 (2001).
[87] B. Godwal, S. Meenakshi, and R. Rao, Phys. Rev. B **56**, 14871 (1997).
[88] N. C. Shekar, D. Polvani, J. Meng, and J. Badding, Physica B **358**, 14 (2005).
[89] H. Marquardt and K. Marquardt, Am. Mineral. **97**, 299 (2012).
[90] H. K. Mao, J. Xu, and P. M. Bell, J. Geophy. Res. **91**, 4673 (1986).
[91] K. Katahara, M. Manghnani, and E. Fisher, J. Appl. Phys. **47**, 434 (1976).

Figure Captions

Figure 1. Phonon dispersions for *bcc*-Ta at ambient and high pressures. Phonon energy as a function of pressure along the high symmetry directions [ξ,0,0] (**a**) and [ξ,ξ,0] (**b**). High-pressure experimental HERIX data in this study were measured at 17.0(5) GPa, 42.0(5) GPa, and 47.0(5) GPa at room temperature, respectively. Data at ambient pressure are taken from [47]. Solid circles represent the LA modes; open circles and triangles denote the TA1 and TA2 modes, respectively. Errors are smaller than the symbol size and not plotted for clarity. The experimental data and errors are listed in Table S1. The black, red, and blue lines represent DFT calculations of the phonon dispersions at 0 GPa, 17.0 GPa, and 47.0 GPa, respectively, where the solid, dashed, and short-dash lines represent the LA, TA1 and TA2 modes, respectively. A significant Kohn anomaly at a reduced wave vector of ~0.7 in LA mode along the Γ-H was observed at 47.0 GPa.

Figure 2. Mode-specific phonon linewidths and the elastic constants of Ta at high pressures. (**a**) Phonon energy and the corresponding phonon linewidth in the LA mode along the Γ-H direction as a function of reduced wave vector at 17.0 and 47.0 GPa, respectively, showing a Kohn anomaly at the phonon wave vector of q = ~0.7 at 47.0 GPa. The dash lines for the phonon linewidth are guides for the eye. **(b)** Elastic constants (C_{ij}) as a function of pressure. Solid symbols represent our single-crystal HERIX results, except the ones at ambient conditions by ultrasonic method [91]. Errors from HERIX measurements are smaller than the symbol size. Open symbols

represent the elastic constants deduced from the sound velocity measurements in powder Ta by IXS in a DAC [41]. The solid lines are our calculated elastic constants for Ta as a function of pressure, which show a softening in both C_{11} and C_{44} at ~100 GPa as indicated by solid-line arrows. The dashed lines represent the calculated elastic constants for electron-doped Ta at high pressures, which show an elastic softening at ~160 GPa as indicated by dashed-line arrows.

Figure 3. Calculated mechanical properties of Ta up to 180 GPa. (**a**) Shear modulus (G), (**b**) Young's modulus (E), (**c**) Bulk modulus (K), and (**d**) Poisson's ratio (v) of Ta at high pressures. These moduli are connected via the equations for isotropic materials: $2G\,(1 + v) = E = 3K\,(1 - 2\,v)$. The results show that the G, E, and K moduli have significant softening anomalies above ~100 GPa, and they drop to minima at around 130 GPa. Correspondingly, the v has a pronounced increase at the similar pressure range.

Figure 4. Calculated phonon dispersions, mode-specific electron-phonon coupling strength, and Fermi-surface nesting function at high pressures. (a) Calculated phonon dispersions for *bcc*-Ta along the high-symmetry directions Γ-H, Γ-N, and Γ-P-H at 0, 17, 47, 110, 200, and 400 GPa, respectively. Calculated mode-specific electron-phonon coupling strength (λ_{qv}) in the LA mode **(b)** and aggregate Fermi-surface nesting function $\xi(\boldsymbol{q})$ **(c)** at 0, 47, and 110 GPa, respectively.

Figure 5. Calculated 3-D Fermi surfaces, band structure, and density of states in *bcc*-Ta. Fermi surfaces of Ta at ambient pressure **(a)** and 110 GPa **(b)**, respectively. An ETT occurs at 110 GPa (red area). ***q*** is the Fermi surface nesting vector along Γ-H shown as red arrows. Calculated electronic band structure at 0 GPa (black lines), 110 GPa (red lines), and 180 GPa (blue lines), respectively **(c)** and projected DOS at 110 GPa (**d**) of Ta. The orange, green and blue colors represent the *s*, *p*, and *d* orbitals in (d), respectively. (**e**) Pressure evolution of band energy across the ETT from 80 to 110 GPa. (**f**) The comparisons of band energy between pristine Ta and electron-doped Ta at 110 GPa. The doped electrons in Ta make the energy band moving down. "+e" represents "doped electrons" in Ta. The position of A and B in the reciprocal space is (0.203, 0.065, 0.203) and (0.301, 0.0969, 0.301) respectively as shown in (b). The Fermi levels are set to be zero energy.

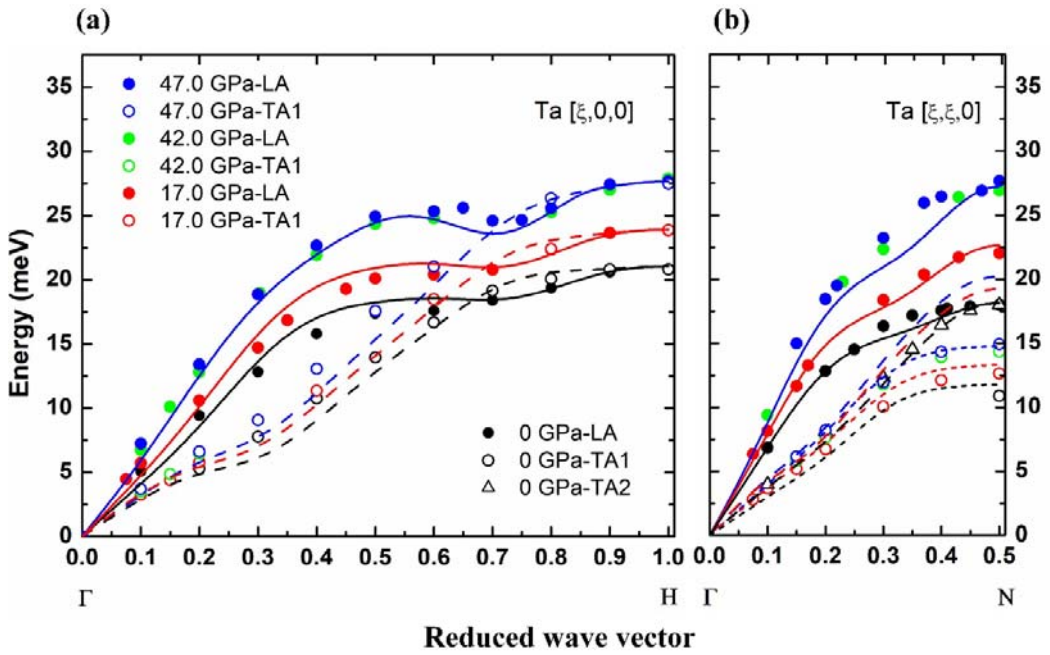
(a)
(b)
47.0 GPa-LA
47.0 GPa-TA1
42.0 GPa-LA
42.0 GPa-TA1
17.0 GPa-LA
17.0 GPa-TA1
0 GPa-LA
0 GPa-TA1
0 GPa-TA2
Ta [ξ,0,0]
Ta [ξ,ξ,0]
Energy (meV)
Γ
H
Γ
N
Reduced wave vector

650

651 **FIG. 1**

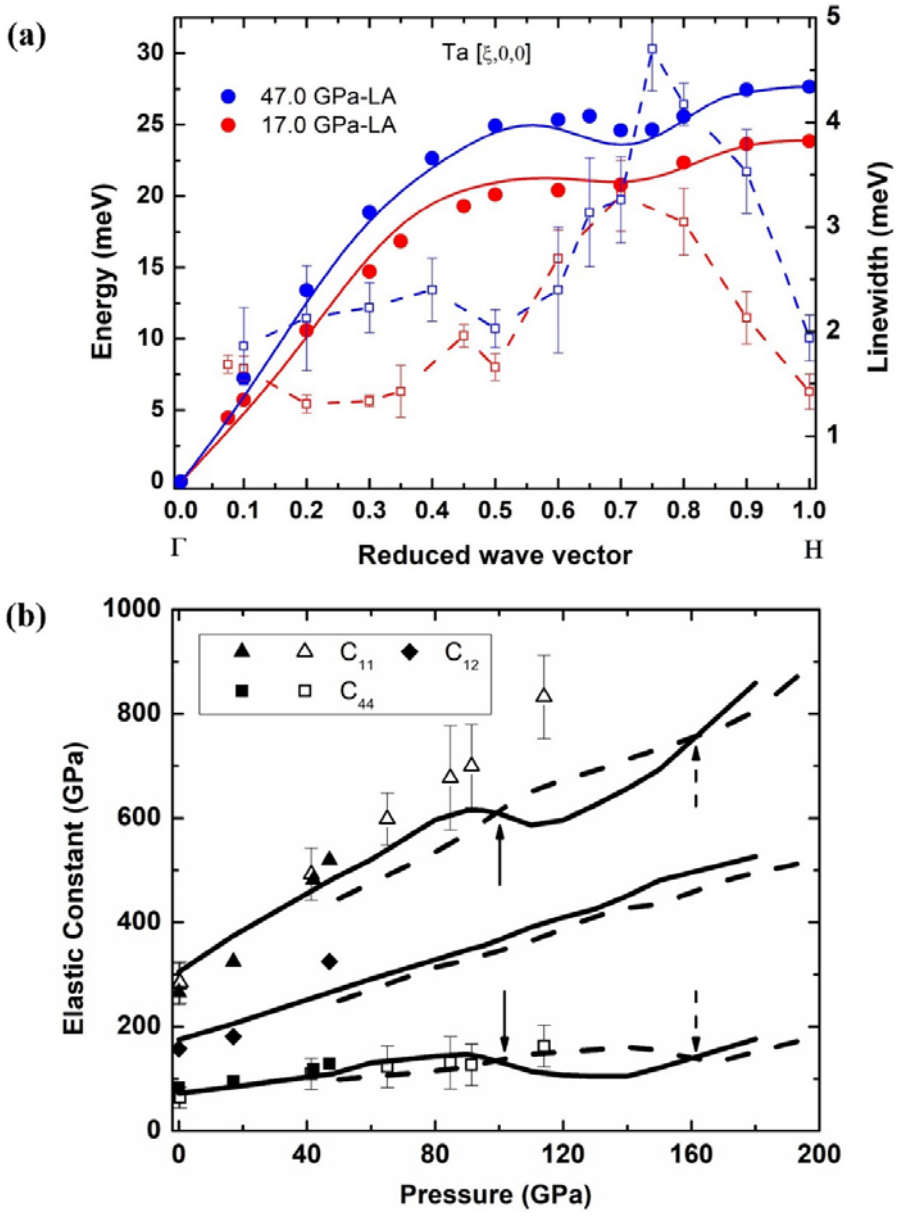
(a)
Ta [ξ,0,0]
47.0 GPa-LA
17.0 GPa-LA
Energy (meV)
Linewidth (meV)
Reduced wave vector
Γ
H
(b)
C11
C12
C44
Elastic Constant (GPa)
Pressure (GPa)

652

653 **FIG. 2**

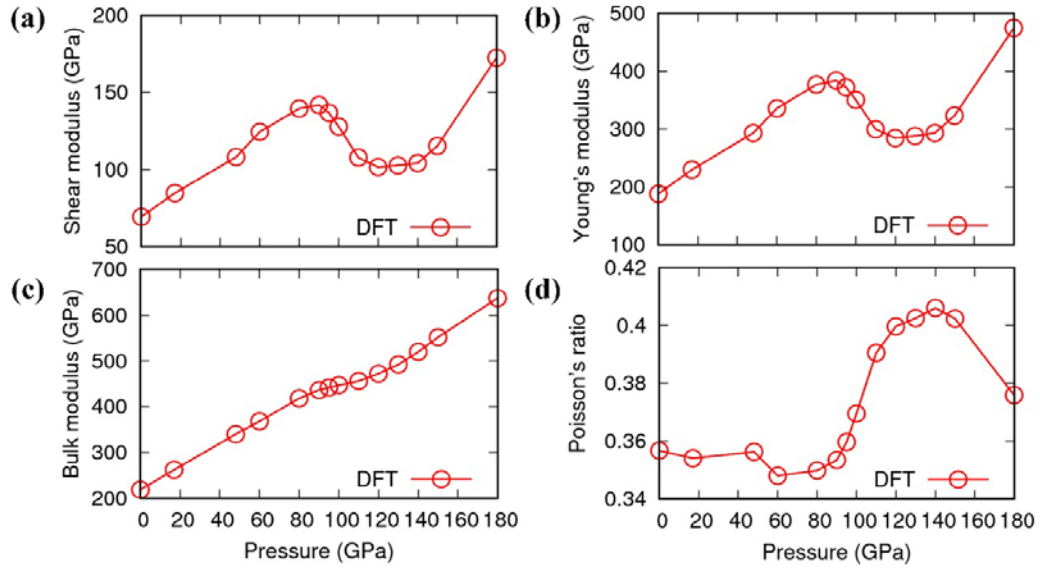

654

655 **FIG. 3**

656

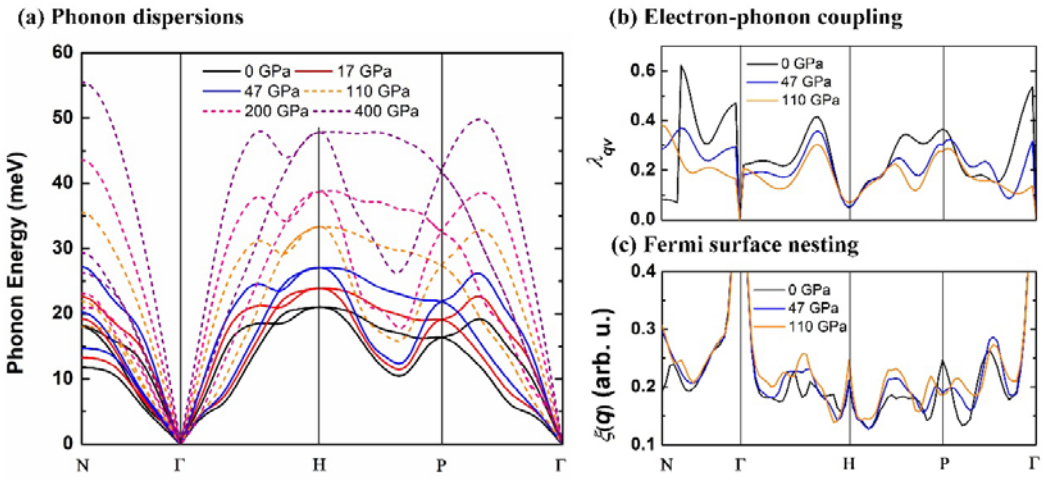

657

658 **FIG. 4**

659

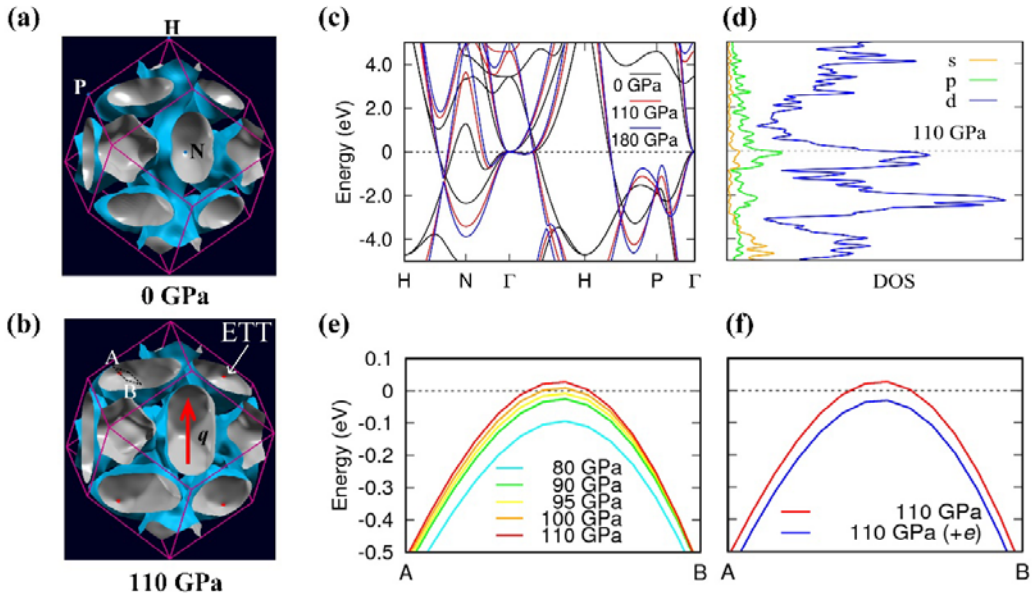
(a)
H
P
N
0 GPa
(b)
ETT
A
B
q
110 GPa
(c)
0 GPa
110 GPa
180 GPa
Energy (eV)
4.0
2.0
0
-2.0
-4.0
H
N
Γ
H
P
Γ
(d)
s
p
d
110 GPa
DOS
(e)
80 GPa
90 GPa
95 GPa
100 GPa
110 GPa
Energy (eV)
0.1
0
-0.1
-0.2
-0.3
-0.4
-0.5
A
B
(f)
110 GPa
110 GPa (+e)
A
B

660

661 **FIG. 5**